

# Facile Synthesis of MnCO<sub>3</sub> Nanoparticles on Ni Foam for Binder-Free Supercapacitor Electrodes

Hui Hua Peng<sup>1</sup>, Liang Zhang<sup>2,\*</sup>, De Yi Jiang<sup>1</sup>, Jie Chen<sup>1,\*</sup>

<sup>1</sup> College of Resources and Environmental Science, State Key Laboratory of Coal Mine Disaster Dynamics and Control, Chongqing University, Chongqing 400044, PR China

<sup>2</sup> College of Aerospace Engineering, Chongqing University, Chongqing 400044, China

\*E-mail: [zhangl@cqu.edu.cn](mailto:zhangl@cqu.edu.cn) (Dr. L. Zhang); [jiechen023@cqu.edu.cn](mailto:jiechen023@cqu.edu.cn) (Dr. J. Chen)

Received: 20 March 2017 / Accepted: 4 May 2017 / Published: 12 June 2017

---

Rhombohedral MnCO<sub>3</sub> nanoparticles were successfully grown on nickel foam via a facile and one-pot water-bath means, wherein the hydrolyzation of urea supplied alkali and carbonate ions. The structure and morphology of the nanocomposites were investigated by XRD, FIB/SEM and elemental mapping. Microscopic investigations revealed MnCO<sub>3</sub> particles with mean sizes that varied from 110-255 nm. EDS mapping showed a homogeneous distribution of manganese, carbon and oxygen. The electrochemical properties of the produced composites were estimated by cyclic voltammetry (CV), galvanostatic charge-discharge (GCD) and electrochemical impedance spectroscopy (EIS) measurements using 6 M KOH as the electrolyte. The resulting electrodes displayed maximum specific capacitance (163.7 F g<sup>-1</sup> at 0.5 A g<sup>-1</sup>), respectable rate capability, and excellent long-term cycling life (91% retention after 1000 cycles). In addition, this manuscript offers us a simple and rapid strategy for the fabrication of electrode materials for use as energy storage devices.

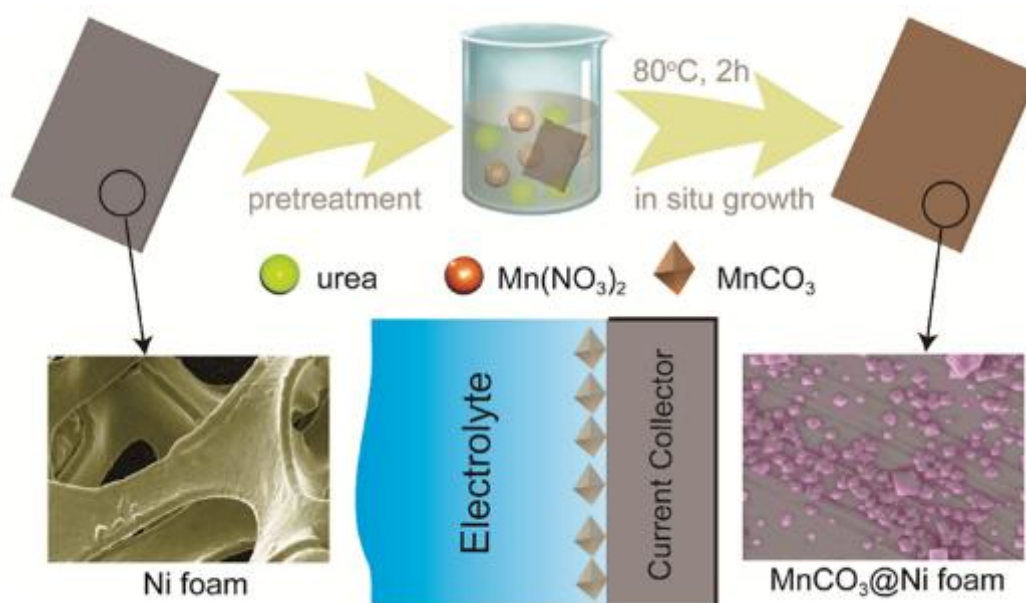
---

**Keywords:** MnCO<sub>3</sub>; urea hydrolysis; electrode materials; supercapacitors

## 1. INTRODUCTION

Recent years, as for energy storage devices, supercapacitors (SCs) or electrochemical capacitors (ECs) have drawn considerable attention due to their commendable pulse charge-discharge characteristics, excellent power density and good cycle-life [1-4]. Depending on the mechanisms of charge storage, SCs are classified as electrical double-layer capacitors (EDLCs) and pseudocapacitors. EDLCs take advantage of charge separation at the electrode/electrolyte interface for charge storage, while pseudocapacitors store energy through the pseudo Faradaic reaction on electrode materials and use double layers for charge storage [5]. For practical applications, SCs are limited by low performance, such as that of carbon-based composites with low specific capacitance [6] or the high

cost of electrode materials, such as  $\text{RuO}_2$  [1]. Therefore, many efforts have been devoted to researching high-capacitance, low-cost and environment-friendly composites. For example, metal oxides/hydroxides ( $\text{MnO}_2/\text{LDH}$ ) [7, 8] and mixed metal oxides ( $\text{NiO-TiO}_2$ ) [9]. However, thus far, their performances of these materials have not been satisfactory due to the extra contact resistance, active species aggregation, and “dead surface” deriving from addition of a conductive agent and a polymer binder during conventional electrode making [10]. Based on the above considerations, one promising route to overcome these problems and achieve enhanced performance is to directly grow active materials on conductive substrates, like Ni foam, for use as integrated electrodes for SCs [8]. Additionally, the synthetic procedures and composites are complicated, so a key challenge is to develop a simple but high-efficiency electrode architecture via facile and controllable synthetic methods. Very recently [8], we have successfully reported a facile one-step way, by which urea hydrolysis supplied alkali and carbonate ions for in situ growth of well-aligned hierarchical Ni-Mn layered double hydroxide nanosheets on a Ni foam surface.



**Scheme 1** Schematic illustration of the in situ growth of  $\text{MnCO}_3$  on the surface of Ni foam.

The use of  $\text{MnCO}_3$  with controllable morphologies, such as peanut-like [11], monodispersed [12], and shuttle-like [13]  $\text{MnCO}_3$  nanostructures, has been most extensively studied due to the abundance of this material in nature and interesting topotactic transformation to  $\text{MnO}_x$  through chemical/thermal conversion [14-18]. The electrochemical characteristics of  $\text{MnCO}_3$  as an active electrode material in a lithium-ion battery have been firstly described [19]. For SCs,  $\text{MnCO}_3$  was initially tested in 0.1 M  $\text{Na}_2\text{SO}_4$ , 0.1 M  $\text{Mg}(\text{ClO}_4)_2$ , and 6 M KOH electrolytes, and exhibited a high specific capacitance of  $216 \text{ F g}^{-1}$  in 0.1 M  $\text{Mg}(\text{ClO}_4)_2$  electrolyte [20]. Later,  $\text{MnCO}_3$  nanospheres ( $129 \text{ F g}^{-1}$ ) and nanocubes ( $91 \text{ F g}^{-1}$ ) were analyzed in 0.1 M  $\text{NaClO}_4$  electrolyte [21]. Because  $\text{MnCO}_3$  is safer and cheaper than  $\text{MnO}_2$ , it may be a potential alternative to  $\text{MnO}_2$  [22]. However, the mechanism of charge storage for  $\text{MnCO}_3$  is not completely understood, and further relevant studies to illustrate the

charge storage mechanism are necessary. Additionally, to the best of our knowledge, the fabrication via urea hydrolysis of  $\text{MnCO}_3@Ni$  foam as electrode material for SCs has not been reported.

In this work, we fabricated  $\text{MnCO}_3$  nanoparticles@Ni foam without binder through a very facile one-step wet-method, illustrated in Scheme 1. The structure, morphology and electrochemical performance of the produced nanocomposites were investigated. The resulting binder-free electrode exhibited good specific capacitance, remarkable rate capability and excellent long-term cycling stability (91% retention after 1000 cycles) suggesting excellent potential application of this material as electrodes for supercapacitors.

## 2. EXPERIMENTAL

### 2.1 Materials and Reagents

Urea and Manganous nitrate (50% solution) were purchased from Aladdin reagent Co. Ltd, Shanghai, China. Other chemicals were purchased from Alfa Aesar. And all used chemicals without further treatment were analytical grade here. Deionized water was used throughout all experimental processes.

### 2.2 Synthesis of $\text{MnCO}_3@Ni$ foam

$\text{MnCO}_3@Ni$  foam composites were synthesized through a very facile water-bath method in a beaker under ambient atmosphere. Typically, a slice of nickel foam ( $2 \times 4 \times 0.1 \text{ cm}^3$ , pore density of 110 PPI, average mass per unit area of  $32 \text{ mg cm}^{-2}$ , purchased from Changsha Lyrun Material Co., Ltd. China) was pretreated with 3 M HCl solution, followed by absolute ethanol and then deionized water in an ultrasound bath for 10 min to remove the NiO layer and residual organics on the surface of the Ni foam. After drying, the Ni foam was immersed in an aqueous solution containing  $\text{Mn}(\text{NO}_3)_2$ , urea and deionized water (60 mL). Then, the mixture was stirred thoroughly for about 10 min to form a homogeneous solution under room conditions. Next, the homogeneous solution was transferred to a water bath kettle at  $80 \text{ }^\circ\text{C}$  for 2 h under vigorously stirring. After the reaction, the beaker was removed and then cooled down to room temperature. Finally, the product was rinsed with DI water and absolute ethyl alcohol for several times, then dried at  $60 \text{ }^\circ\text{C}$  overnight.

Three different concentrations of  $\text{Mn}^{2+}$  were tested, 2, 5 and 10 mmol (denoted as M2, M5 and M10, respectively). in the initial addition of the reagent. The molar ratio of the feeding metal ion ( $\text{Mn}^{2+}$ )/urea was 1/3.3. The average mass loading of active materials for M2, M5 and M10 were about 2, 3 and 4 mg, respectively.

### 2.3 Materials characterization

Focused-ion-beam scanning electron microscopy (FIB/SEM) with an accelerating voltage of 20 kV was used to characterize the morphological and structural information of the produced samples. An energy dispersive X-ray spectroscope (EDX) attached to the FIB/SEM was applied to analyze elements distribution. The crystallographic information and chemical composition of the products were analyzed

by powder X-ray diffraction with a scan step of  $0.02^\circ$  and a scan range between  $5^\circ$  and  $80^\circ$  (XRD, Rigaku D/max 2500, Cu  $K\alpha$ ).

#### 2.4 Electrochemical measurement

Electrochemical performance of all produced electrodes were measured by means of an electrochemical workstation (CHI 660E, Chenhua, Shanghai) within a three-electrode cell configuration containing 6 M KOH aqueous solution at room temperature.  $\text{MnCO}_3@\text{Ni}$  foam ( $1 \times 1.5 \text{ cm}^2$ ) samples were directly used as working electrode. And a saturated Hg/HgO electrode (SCE) and a platinum plate were selected as the reference and counter electrodes, respectively. The specific capacitances ( $C_m$ ) of all electrodes were calculated from the galvanostatic charge–discharge curves, as follows:

$$C_m = \frac{I\Delta t}{m\Delta U} \quad (1)$$

where  $I$  (A) represents the discharge current,  $\Delta t$  (s) refers to the discharge time,  $\Delta U$  (V) denotes the voltage range, and  $m$  (g) is the mass of the electroactive materials on the nickel foam. Cyclic voltammetry (CV) measurements (within the potential window of 0-0.4 V), galvanostatic charge-discharge (GCD) tests, and electrochemical impedance spectroscopy (EIS) tests were all performed on this electrochemical workstation. EIS tests were performed with a perturbation amplitude of 5 mV in the frequency range from 100000 Hz to 0.01 Hz.

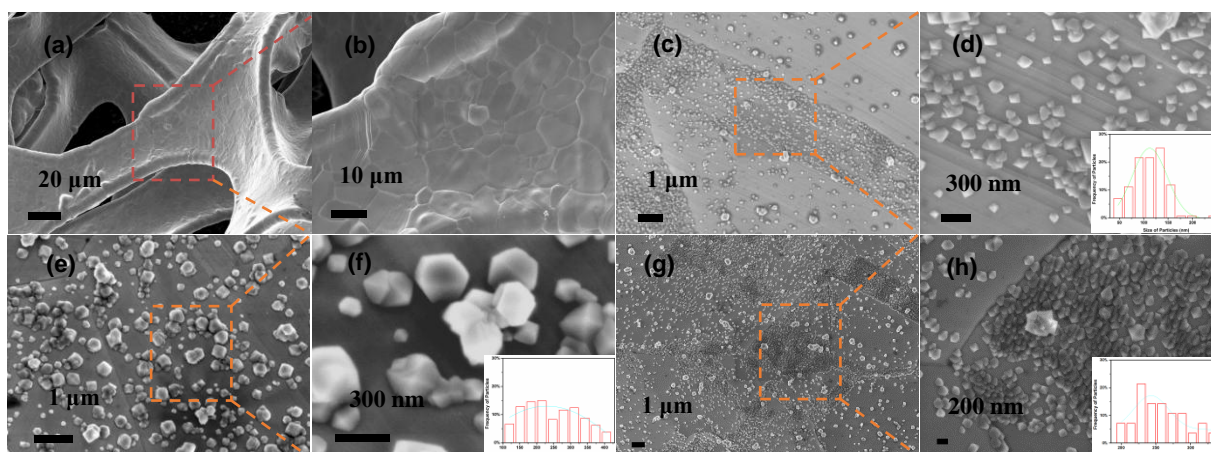


**Figure 1.** SEM images of (a)-(b) the bare Ni foam after pretreated treatment; (c)-(d) M2; (e)-(f) M5; (g)-(h) M10. (b), (d), (f) and (h) are the enlarged parts of (a), (c), (e) and (g), respectively. The insets show the corresponding particle distributions.

### 3. RESULTS AND DISCUSSION

#### 3.1 Structure and morphology

Representative SEM images of the bare Ni foam after pre-treatment, M2, M5 and M10 are presented in Fig. 1. As shown in Fig. 1a-b, the Ni foam surface appeared very smooth without any

impurities after pre-treatment, which is beneficial for the growth of three-dimensional structure composites. After being covered with  $\text{MnCO}_3$  nanoparticles, the 3D framework of the nickel foam was well-retained (Fig. 2a), and the Ni foam surface was rougher than the bare nickel foam (Fig. 1c-h). Obviously, the as-obtained samples consisted of pure rhombohedral structure and were uniformly deposited on the nickel foam surface, suggesting that the urea hydrolysis system allows growth of homogeneous  $\text{MnCO}_3$  nanoparticles on Ni foam. However, without Ni foam support, the  $\text{MnCO}_3$  particles appeared heavily aggregated, as seen from the SEM image of powder  $\text{MnCO}_3$  particles (obtained from the precipitate, Fig. 2b). The results indicated that the Ni foam not only acts as the current collector, but also serves as a carrier to support  $\text{MnCO}_3$  nanoparticles that are immobilized on the surface of the Ni foam. However, we observed that the  $\text{MnCO}_3$  nanoparticles were bigger (mean diameter from  $\sim 110$  nm to  $\sim 255$  nm) and slightly self-aggregated as the feeding contents of  $\text{Mn}^{2+}$  increased, which may have impeded the charge transportation from the active materials to the current collector and reduced the ion diffusion at the electrolyte/electrode interface, resulting in poor electrochemical performance. Furthermore, the insets of Fig. 1 (d), (f) and (h) show the corresponding particle distributions, as processed by Nano Measurer software.

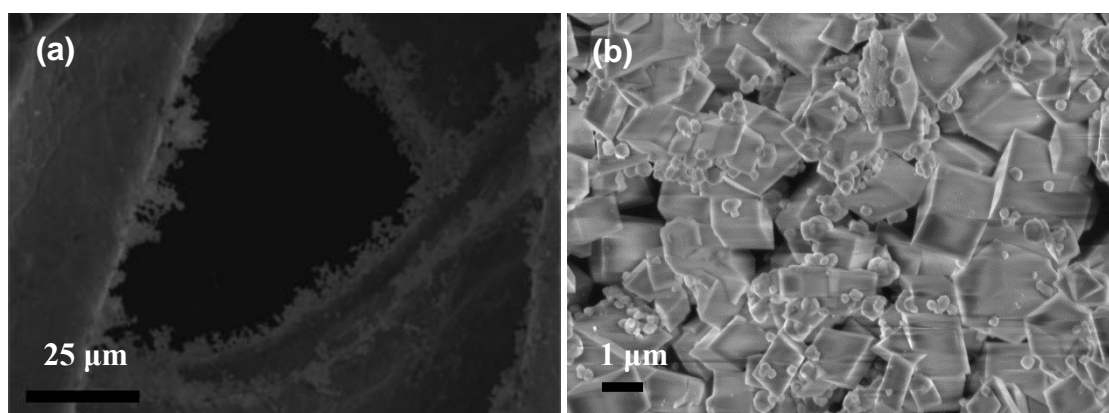


**Figure 2.** (a) Overview SEM image of Ni foam with  $\text{MnCO}_3$ , and (b) SEM image of powder  $\text{MnCO}_3$  particles.

Furthermore, to investigate the crystal structure of samples, XRD measurements were conducted and XRD patterns of all samples are shown in Fig. 3b. Except for the obvious diffraction peaks originating from Ni foam (JCPDS No. 65-2865), the diffraction peaks of  $\text{MnCO}_3$  were weak because of a lower amount of materials. However, the well-defined diffraction peaks at  $2\theta = 24.25^\circ$ ,  $31.36^\circ$ ,  $37.52^\circ$ ,  $65.43^\circ$  and  $77.94^\circ$  could be successfully indexed to a series of (012), (104), (110), (208), and (128) planes, respectively, which are consistent with the previously reported patterns for the  $\text{MnCO}_3$  phases (JCPDS No. 44-1472) [15]. And no other crystalline phases were discovered, suggesting high purity of the  $\text{MnCO}_3$  nanoparticles. These results confirmed that the  $\text{MnCO}_3$  nanoparticles successfully grew on the surface of the nickel foam.

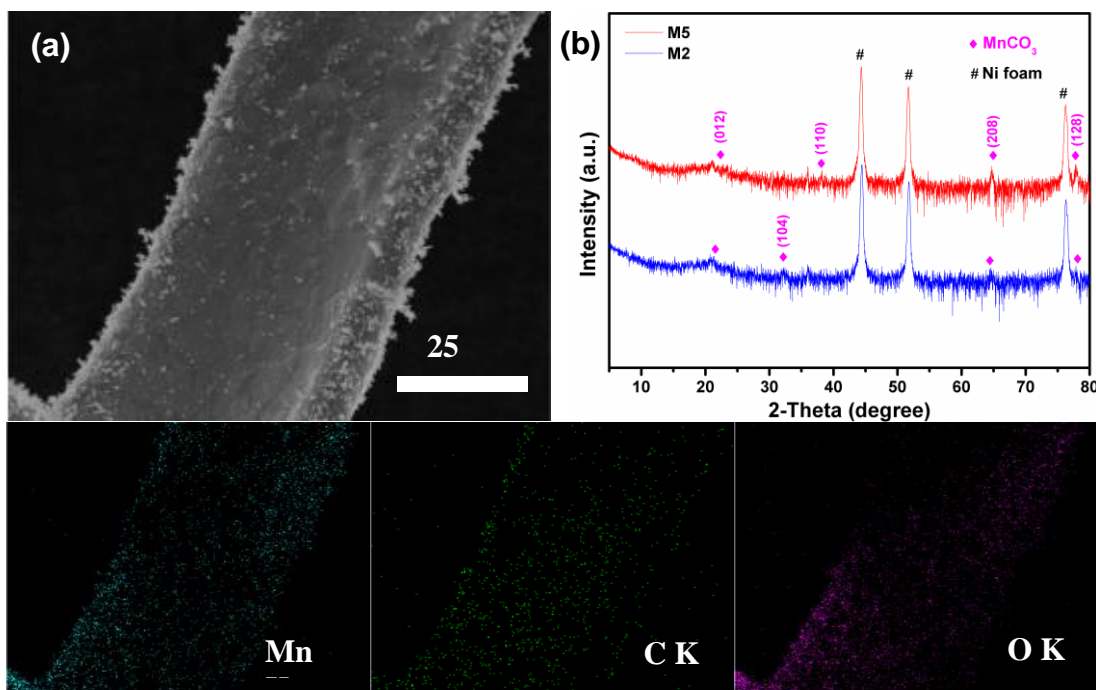
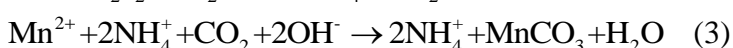
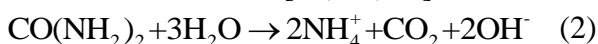


**Figure 3.** (a) EDS mapping of Mn, C and O elements in a surface of MnCO<sub>3</sub>@Ni foam, and (b) XRD patterns of as-obtained samples M2 and M5.

The EDS spectrums (Fig. 3a) also revealed the presence of Mn, C and O unambiguously, and indicated that the MnCO<sub>3</sub>@Ni foam had a homogeneous distribution of Mn, C and O throughout the nickel foam network. According to the above-mentioned results, the formation mechanism of MnCO<sub>3</sub> may be illustrated as follows [16, 23, 24]:



The carbonate anions in the synthesis were provided by hydrolyzation of urea (Eqn (2)) when the reaction temperature increased above 60 °C [17]. And according to the literature [23], a certain amount of H<sub>2</sub>O in the synthetic mixture plays an important role in forming MnCO<sub>3</sub> crystals (Eqn (3)).

### 3.2 Electrochemical behavior

The cyclic voltammetry (CV) curves of M2 at various scan rates varying from 5-100 mV s<sup>-1</sup> are presented in Fig. 4a. The current increased with increasing scan rate, and the well-defined redox peaks within 0 to 0.4 V were evident in all CV curves. The shape of the CV curves clearly revealed the pseudocapacitive characteristics derived from the Faradaic reactions. A couple of highly reversible redox peaks were located at around 0.123 and 0.179 V at low scan rate, 5 mV s<sup>-1</sup>. As the sweep rate enhanced from 5 to 100 mV s<sup>-1</sup> (twentyfold increase), the potential values of the anodic peak and cathodic peak shifted slightly from 0.179 to 0.195 V and 0.123 to 0.113 V respectively, indicating a relatively low resistance of the electrode due to the good contact between the MnCO<sub>3</sub> nanoparticles and the conductive nickel foam substrate [25]. Fig. 4b shows the galvanostatic charge-discharge (GCD) curves of M2 at different current densities (0.5-5 A g<sup>-1</sup>). According to eqn (1), the specific

capacitance ( $C_m$ ) can be calculated from discharge curves, resulting in 163.7, 158, 149.7, 145.7 and 141.4  $F g^{-1}$  at 0.5, 1, 2, 3 and 5  $A g^{-1}$ , respectively. Almost 86.4% of the capacitance was retained for the sample as the discharge current density increased from 0.5 to 5  $A g^{-1}$  (10-fold increase), indicating its excellent rate capability (Fig. 4e). This performance is remarkable compared with previous reports for  $MnCO_3$  electrode, as shown in Table 1 [20, 21]. For instance, Devaraj and co-workers first obtained a specific capacitance of 159  $F g^{-1}$  at 0.5 mA current for  $MnCO_3$  particles electrode in 6 M KOH electrolyte [20]. More recently, Zhang and his collaborators utilized ethylene glycol to synthesize  $MnCO_3$  nanospheres and nanocubes using a precipitation method and obtained specific capacitances of 129  $F g^{-1}$  and 91  $F g^{-1}$  at the discharge current density of 0.15  $A g^{-1}$  in 0.1 M  $NaClO_4$  electrolyte for  $MnCO_3$  nanospheres and nanocubes electrodes, respectively. However, these reported rate capacity values were low because of the relatively large charge-transfer resistances [21].

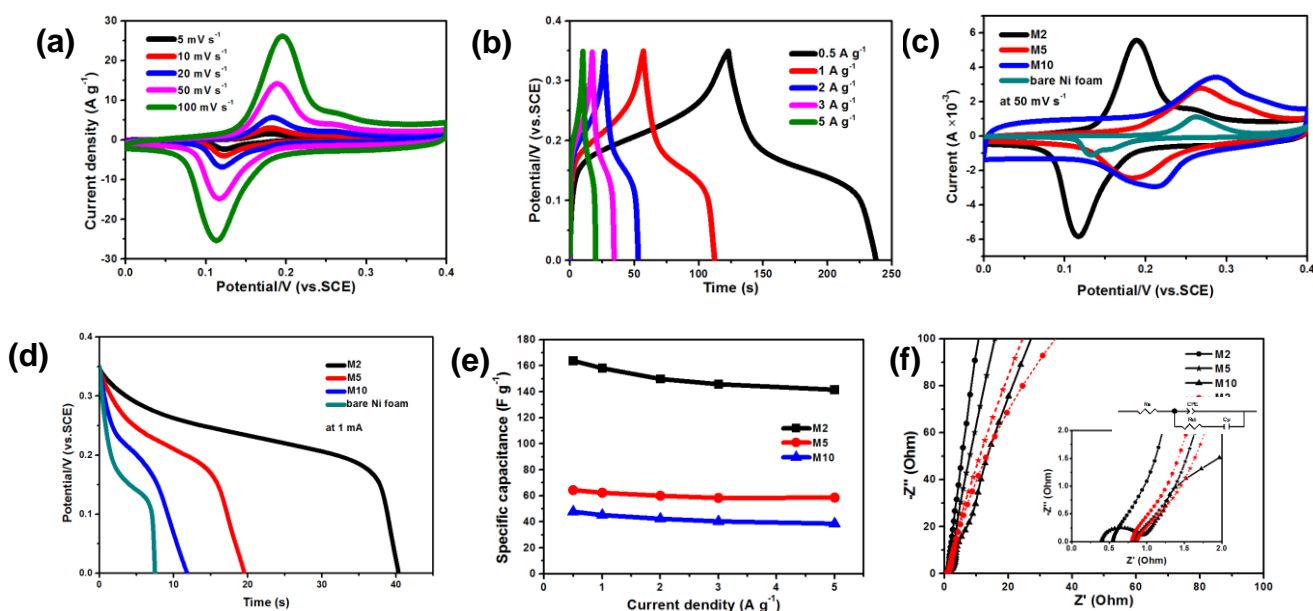


**Figure 4.** (a) Cyclic voltammograms for M2 at different scan rates; (b) Charge-discharge curves for M2 at different current densities; Comparisons of (c) CV curves at 50  $mV s^{-1}$  and (d) galvanostatic charge-discharge curves at 1 mA of M2, M5, M10 and bare Ni foam; (e) Specific capacitance under different current densities, and (f) Nyquist plots before (black solid line) and after (red dash line) circulation. The insets show the enlarged part of EIS and equivalent circuit.

The CV and GCD curves of M5 and M10 under identical conditions are illustrated in Fig. 5, and the data show that these materials demonstrate similar electrochemical behaviors to those of M2. However, the specific capacitances of M5 obtained from discharge curves are 64.3, 62.3, 60, 58.3 and 58.6  $F g^{-1}$  at 0.5, 1, 2, 3 and 5  $A g^{-1}$ , respectively, and that of M10 are 47.7, 45.1, 42.3, 40.3 and 38.6  $F g^{-1}$ , respectively, lower than those of M2. Moreover, Fig. 4c compares the CV curves of samples at the scan rates of 50  $mV s^{-1}$ . Obviously, the sample M2 shows the largest enclosed area of the CV curves. Besides, the comparisons of GCD curves for different samples at 1 mA current are presented in Fig. 4d. The nonlinear and symmetric charge-discharge curves confirm the faradaic behavior and suggest good electrochemical reversibility and high coulombic efficiency. What's more, sample M2 showed a longer discharge time, in coincidence with the above analytical results. As discussed above, use of

lower concentration for  $\text{Mn}^{2+}$  feeding resulted in better specific capacitance (Fig. 4c-e). This is not only due to the lower loading of active material but also the slight self-aggregation of  $\text{MnCO}_3$  particles, resulting in condensed packing of active species (see SEM results), though the thickness of active materials may increase with the increase of feeding contents. Therefore, loading at a lower concentration results in higher value of specific capacitance because of the higher utilization of active material, as described in previous works [22, 26, 27]. However, the rate capabilities of all samples are respectable, 86.4%, 91.1% and 80.9% retained at  $5 \text{ A g}^{-1}$  for M2, M5 and M10, respectively (Fig. 4e), implying that  $\text{MnCO}_3$  nanoparticles are relatively stable. Additionally, it may be important to subtract the contribution of the bare Ni foam. It is shown that Ni foam itself has negligible current response (Fig. 4c-d), which is consistent with observations in previously reported literatures [8, 21, 28]. Therefore, the specific capacitance contribution from the nickel foam current collector can be ignored.

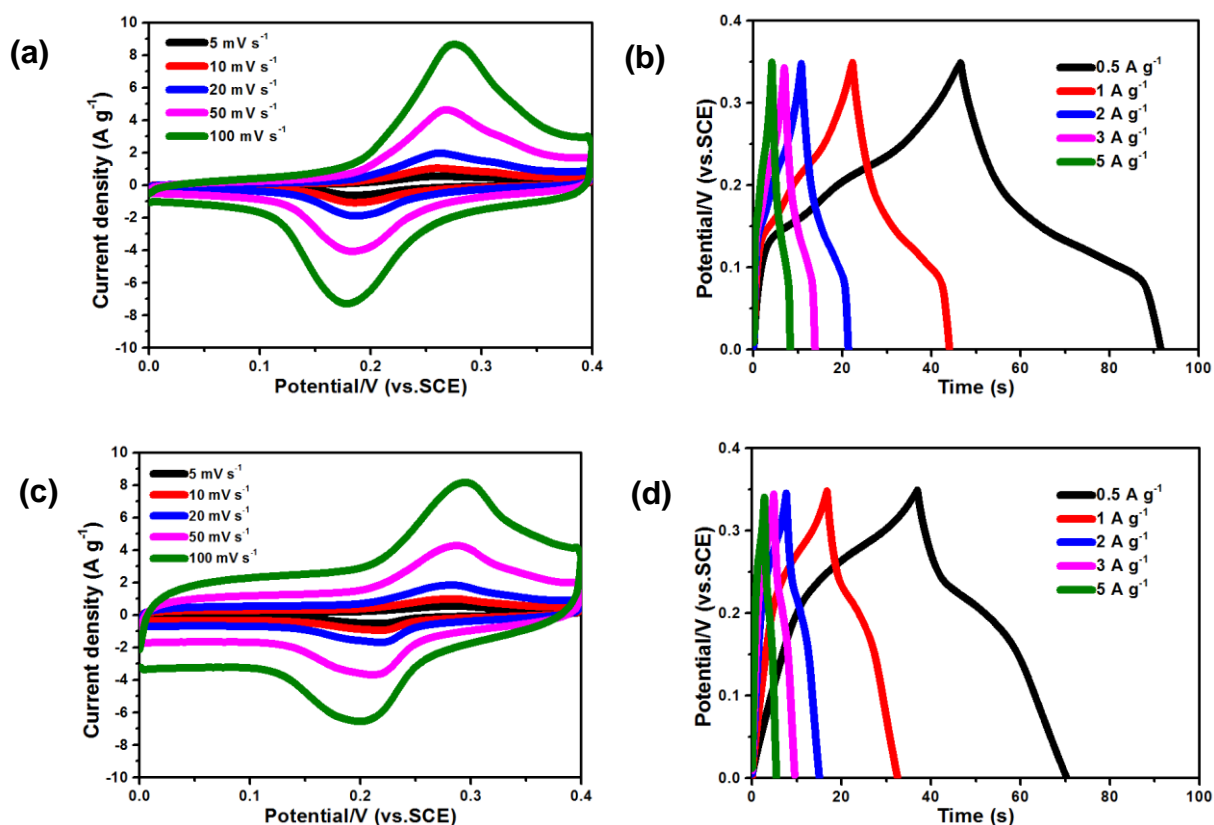


**Figure 5.** Cyclic voltammograms at different scan rates and charge-discharge curves at different current densities for (a-b) M5 and (c-d) M10.

The electrochemical behavior was further investigated by electrochemical impedance spectroscopy (EIS) over the frequency range 0.01 Hz-100 kHz (Fig. 4f). The Nyquist plots were used to analyze the EIS data. At high frequencies, the intercept in the real part ( $Z'$ ) was a combinational resistance ( $R_s$ ) of intrinsic resistance of the substrate, ionic resistance of the electrolyte, and contact resistance at the active materials/current collector interface. In the high-frequency range, the semicircle diameter of EIS represents the charge-transfer resistance ( $R_{ct}$ ) caused by the Faradic reaction and the double-layer capacitance on the grain surface. According to the equivalent circuit (inset of Fig. 4f,

where  $C_p$  is a pseudocapacitive element from the redox process, and CPE is a constant phase element to account for the double-layer capacitance), the  $R_s$  of samples as calculated by the Zview software were all very small, i.e. only 0.5  $\Omega$ , 0.8  $\Omega$ , and 0.4  $\Omega$  for M2, M5, and M10 before circulation, respectively. The impedance spectrum was an approximate vertical line to the real axis, suggesting high values of  $R_{ct}$ . However, the ion diffusive resistance of M2 was lower due to the higher slope of the straight line in the low frequency region [29]. These results show good agreement with the CV and GCD behaviors for these materials, demonstrating that  $MnCO_3$  nanoparticles@Ni foam exhibits good contact and charge transportation between the conducting substrate and active materials, and the use of the lower concentration for feeding resulted in M2 sample that showed better ion diffusive resistance and lower combinational resistance.

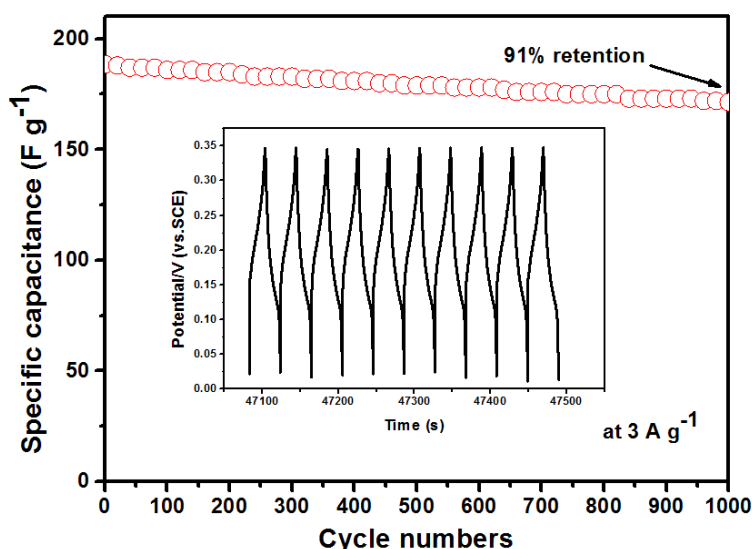
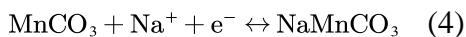


**Figure 6.** Cycling performance of M2 at the current density of 3 A g<sup>-1</sup>. The inset is the galvanostatic charging-discharge curves of last 10 cycles.

Long-term cyclic stability is a key property for supercapacitor practical applications. Fig. 6 displays the long-term cycling life measurement at 3 A g<sup>-1</sup> for sample M2. The specific capacitance remained about 91% even after 1000 cycles, which reflects an excellent long-term stability of electrochemical performance. And the result was further confirmed by the stable and reversible charge/discharge curves at the last 10 cycles, displaying similar potential-time response behavior for each charge/discharge curve (inset of Fig. 6). Comparatively, the cycling capability of sample M5 was retained at 80% after 1000 cycles, as is shown in Fig. 7. In addition, the EIS of  $MnCO_3$  nanoparticles@Ni foam electrodes after 1000 cycles were also measured (red dashed line, Fig. 4f), which displayed similar impedance spectra as those 1000 cycles before. The  $R_s$  of M2 electrode only changed slightly, from 0.5 to 0.8  $\Omega$  after 1000 cycles, showing good conductivity of the electrolyte and low internal resistance of the electrode. There was only a slight decrease of the straight line slope in the low frequency region after 1000 cycles. Hence, these findings illustrate that the  $MnCO_3$  nanoparticles@Ni foam electrodes have potential for use as high-performance energy storage materials.

Debasis et al. recommended that the pseudocapacitive mechanism of  $\text{MnCO}_3$  in  $\text{Na}_2\text{SO}_4$  electrolyte could be considered as [30]:



However, Devaraj et al. argued that the charge storage by intercalation/deintercalation of alkali metal ions and/or protons from/into  $\text{MnCO}_3$  is very unlikely, because the oxidation state of Mn in  $\text{MnCO}_3$  is +2 unlike  $\text{MnO}_2$  (where the oxidation state of Mn is in +4), limiting charge storage. The high value of SC can not only be attributed to the adsorption/desorption of protons and/or alkali metal ions on the surface [20]. In this work,  $\text{MnCO}_3$  nanoparticles@Ni foam exhibited remarkable pseudocapacitive behavior, indicating the potential application as an energy storage material. However, more detailed study on the charge storage mechanism of  $\text{MnCO}_3$  is required.

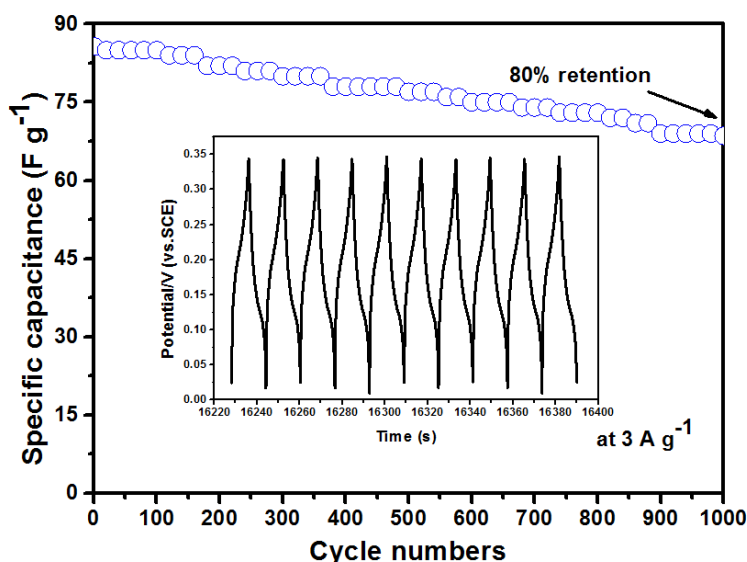


**Figure 7.** Cycling performance of M5 at the current density of  $3 \text{ A g}^{-1}$ . The inset is the galvanostatic charge/discharge curves of last 10 cycles.

**Table 1.** Comparisons of electrochemical properties with similar electrode materials reported in previous literatures for supercapacitors.

Materials	Electrolytes	$C_m / \text{F g}^{-1}$	Rate capability	Cycling life (cycling numbers)	References
$\text{MnCO}_3$ particles	0.1 M $\text{Na}_2\text{SO}_4$	3 (at 0.5 mA)	-	-	[20, 22]
	0.1 M $\text{Mg}(\text{ClO}_4)_2$	216 (at 0.5 mA)	15% (at 10 mA)	90.3% (500)	
	6 M KOH	159 (at 0.5 mA)	-	-	
$\text{MnCO}_3$ nanospheres	0.1 M $\text{NaClO}_4$	129 (at $0.15 \text{ A g}^{-1}$ )	<50% (at $2 \text{ A g}^{-1}$ )	87% (1000)	[21]
		$\text{MnCO}_3$ nanocubes	91 (at $0.15 \text{ A g}^{-1}$ )	<50% (at $2 \text{ A g}^{-1}$ )	
$\text{MnCO}_3$	1 M $\text{Na}_2\text{SO}_4$	99 (at $9 \text{ A g}^{-1}$ )	53.5% (at $9 \text{ A g}^{-1}$ )	92% (1000)	[30]
$\text{MnCO}_3$ nanoparticles @Ni foam (M2)	6 M KOH	163.7 (at $0.5 \text{ A g}^{-1}$ )	86.4% (at $5 \text{ A g}^{-1}$ )	91% (1000)	This work

#### 4. CONCLUSIONS

In summary, the rhombohedral  $\text{MnCO}_3$  nanoparticles were successfully fabricated on the nickel foam via a one-pot, very facile water-bath method using urea as alkali and carbonate ion source. In this case, the  $\text{MnCO}_3$  nanoparticles played the role of active species and the Ni foam served as both support and electron collector. The resulting electrode exhibited a good specific capacitance ( $163.7 \text{ F g}^{-1}$  at  $0.5 \text{ A g}^{-1}$ ), great rate capacity, and excellent long-term cyclic stability. These results implied that  $\text{MnCO}_3$  nanoparticles@Ni foam could potentially be used as a selectable electrochemical energy storage devices materials or other applications. Additionally, this manuscript presented a facile and well-suited method, which could be readily extended for the synthesis of other nanocomposites.

#### ACKNOWLEDGEMENTS

The authors gratefully acknowledge the financial supports provided by National Natural Science Foundation of China (Grant no. 61474011). We are grateful to National Natural Science Foundation of China (Grant no. 41672292, 51604044, and 51574048), State Key Laboratory of Coal Mine Disaster Dynamics and Control (2011DA105287-FW201504) Chongqing science and technology commission (Grant No. cstc2015jcyjA90011), International S&T Cooperation Projects of Chongqing (CSTC2013gjh90001) and the Fundamental Research Funds for the Central Universities (No. 106112016CDJZR245518 and 106112016CDJZR135506) for supporting this project.

#### References:

1. J.R. Miller, P. Simon, *Science*, 321 (2008) 651.
2. P. Simon, Y. Gogotsi, *Nat. Mater.*, 7 (2008) 845.
3. P. Simon, Y. Gogotsi, B. Dunn, *Science*, 343 (2014) 1210.
4. M. Huang, F. Li, F. Dong, Y.X. Zhang, L.L. Zhang, *J. Mater. Chem. A*, 3 (2015) 21380.
5. A. Yu, A. Davies, Z. Chen, *Wiley-VCH Verlag GmbH & Co. KGaA*, 7(2011):21.
6. M. Inagaki, H. Konno, O. Tanaike, *J. Power Sources*, 195 (2010) 7880.
7. P.D. Zeng, X.Z. Yu, D.H. Xiao, Q.W. Zhong, *Ceram. Int.*, 40 (2014) 2115.
8. X.L. Guo, X.Y. Liu, X.D. Hao, S.J. Zhu, F. Dong, Z.Q. Wen, Y.X. Zhang, *Electrochim. Acta*, 194 (2016) 179.
9. J.H. Kim, K. Zhu, Y. Yan, C.L. Perkins, A.J. Frank, *Nano Lett.*, 10 (2010) 4099.
10. G.Q. Zhang, H.B. Wu, H.E. Hoster, M.B. Chanpark, W.L. Xiong, *Energy Environ. Sci.*, 5 (2012) 9453.
11. Y. Tang, S. Chen, T. Chen, W. Guo, Y. Li, S. Mu, S. Yu, Y. Zhao, F. Wen, F. Gao, *J. Mater. Chem. A*, 5 (2017) 3923.
12. S. Wang, Q. Li, W. Pu, Y. Wu, M. Yang, *Ionics*, 22 (2016) 771.
13. X. Sun, Z. Li, Y. Cheng, L. Xue, *ECS J. Solid State Sci. Technol.*, 6 (2017) R63.
14. X. Ge, C.D. Gu, X.L. Wang, J.P. Tu, *J. Colloid Interface Sci.*, 438 (2015) 149.
15. H. Hu, J.Y. Xu, H. Yang, J. Liang, S. Yang, H. Wu, *Mater. Res. Bull.*, 46 (2011) 1908.
16. L. Liu, Z. Yang, H. Liang, H. Yang, Y. Yang, *Mater. Lett.*, 64 (2010) 2060.
17. S. Lei, Z. Liang, L. Zhou, K. Tang, *Mater. Chem. Phys.*, 113 (2009) 445.
18. X. Wang, Y. Li, *Mater. Chem. Phys.*, 82 (2003) 419.
19. M.J. Aragón, B. León, C.P. Vicente, J.L. Tirado, *J. Power Sources*, 196 (2011) 2863.
20. S. Devaraj, H.Y. Liu, P. Balaya, *J. Mater. Chem. A*, 2 (2014) 4276.
21. N. Zhang, J. Ma, Q. Li, J. Li, D.H.L. Ng, *Rsc Adv.*, 5 (2015) 81981.

22. S. Devaraj, P.V. Vardhan, H.Y. Liu, P. Balaya, *J. Solid State Electrochem.*, 20 (2016) 1877.
23. L. Liu, X. Zhang, R. Wang, J. Liu, *Superlattices Microstruct.*, 72 (2014) 219.
24. E.M. Nour, S.M. Teleb, N.A. AL-Khsosy, M.S. Refat, *Synth. React. Inorg., Met.-Org., Nano-Met. Chem.*, 27 (1997) 505.
25. G.Q. Zhang, X.W. Lou, *Adv. Mater.*, 25 (2013) 976.
26. Z.N. Yu, B. Duong, D. Abbitt, J. Thomas, *Adv. Mater.*, 25 (2013) 3302.
27. L. Yuan, X.H. Lu, X. Xiao, T. Zhai, J. Dai, F. Zhang, B. Hu, X. Wang, L. Gong, J. Chen, C. Hu, Y. Tong, J. Zhou, Z.L. Wang, *ACS Nano*, 6 (2012) 656.
28. Z. Liu, K. Xu, H. Sun, S. Yin, *Small*, 11 (2015) 2182.
29. L. Zhang, M. Ou, H. Yao, Z. Li, D. Qu, F. Liu, J. Wang, J. Wang, Z. Li, *Electrochim. Acta*, 186 (2015) 292.
30. D. Ghosh, S. Giri, S. Dhibar, C.K. Das, *Electrochim. Acta*, 147 (2014) 557.

© 2017 The Authors. Published by ESG ([www.electrochemsci.org](http://www.electrochemsci.org)). This article is an open access article distributed under the terms and conditions of the Creative Commons Attribution license (<http://creativecommons.org/licenses/by/4.0/>).